Published in final edited form as:
Mol Imaging Biol. 2012 April ; 14(2): 213–224. doi:10.1007/s11307-011-0485-3.

Pharmacokinetics, Metabolism, Biodistribution, Radiation Dosimetry, and Toxicology of ^{18}F-Fluoroacetate (^{18}F-FACE) in Non-human Primates

Ryuichi Nishii[1,4], **William Tong**[1], **Richard Wendt III**[2], **Suren Soghomonyan**[1], **Uday Mukhopadhyay**[1], **Julius Balatoni**[1], **Osama Mawlawi**[2], **Luc Bidaut**[2,5], **Peggy Tinkey**[3], **Agatha Borne**[3], **Mian Alauddin**[1], **Carlos Gonzalez-Lepera**[1], **Bijun Yang**[1], and **Juri G. Gelovani**[1]

[1]Department of Experimental Diagnostic Imaging, Center for Advanced Biomedical Imaging Research (CABIR), UT M. D. Anderson Cancer Center, 1881 East Road 3SCR2.3924, Houston, TX 77054, USA

[2]Department of Imaging Physics, UT M. D. Anderson Cancer Center, Houston, TX, USA

[3]Department of Veterinary Medicine & Surgery, UT M. D. Anderson Cancer Center, Houston, TX, USA

[4]Moriyama 5-4-30, Moriyama-shi, Shiga 524-8524, Japan

[5]Centre for Oncology & Molecular Medicine, Ninewells Hospital and Medical School, University of Dundee, James Arrott Drive, Dundee DD1 9SY, Scotland UK

Abstract

Introduction—To facilitate the clinical translation of ^{18}F-fluoroacetate (^{18}F-FACE), the pharmacokinetics, biodistribution, radiolabeled metabolites, radiation dosimetry, and pharmacological safety of diagnostic doses of ^{18}F-FACE were determined in non-human primates.

Methods—^{18}F-FACE was synthesized using a custom-built automated synthesis module. Six rhesus monkeys (three of each sex) were injected intravenously with ^{18}F-FACE (165.4± 28.5 MBq), followed by dynamic positron emission tomography (PET) imaging of the thoracoabdominal area during 0–30 min post-injection and static whole-body PET imaging at 40, 100, and 170 min. Serial blood samples and a urine sample were obtained from each animal to determine the time course of ^{18}F-FACE and its radiolabeled metabolites. Electrocardiograms and hematology analyses were obtained to evaluate the acute and delayed toxicity of diagnostic dosages of ^{18}F-FACE. The time-integrated activity coefficients for individual source organs and the whole body after administration of ^{18}F-FACE were obtained using quantitative analyses of dynamic and static PET images and were extrapolated to humans.

Results—The blood clearance of ^{18}F-FACE exhibited bi-exponential kinetics with half-times of 4 and 250 min for the fast and slow phases, respectively. A rapid accumulation of ^{18}F-FACE-derived radioactivity was observed in the liver and kidneys, followed by clearance of the radioactivity into the intestine and the urinary bladder. Radio-HPLC analyses of blood and urine samples demonstrated that ^{18}F-fluoride was the only detectable radiolabeled metabolite at the level of less than 9% of total radioactivity in blood at 180 min after the ^{18}F-FACE injection. The uptake of free ^{18}F-fluoride in the bones was insignificant during the course of the imaging studies.

Correspondence to: Juri G. Gelovani; jgelovani@mdanderson.org.
Ryuichi Nishii and William Tong contributed equally to this work.

Conflict of Interest Disclosure. The authors declare that they have no conflict of interest.

No significant changes in ECG, CBC, liver enzymes, or renal function were observed. The estimated effective dose for an adult human is 3.90–7.81 mSv from the administration of 185–370 MBq of ^{18}F-FACE.

Conclusions—The effective dose and individual organ radiation absorbed doses from administration of a diagnostic dosage of ^{18}F-FACE are acceptable. From a pharmacologic perspective, diagnostic dosages of ^{18}F-FACE are non-toxic in primates and, therefore, could be safely administered to human patients for PET imaging.

Keywords

^{18}F-Fluoroacetate; Positron emission tomography; Radiation dosimetry; Toxicology; Non-human primate

Introduction

Positron emission tomography (PET) with ^{18}F-fluorodeoxyglucose (^{18}F-FDG) has become a widely used molecular imaging method for diagnosis and staging of several tumor types and for monitoring the efficacy of different anti-cancer therapeutic interventions [1–4]. Examples of ^{18}F-FDG-avid tumor types include cancers of the head and neck, lung, breast, and malignant lymphoma. For these, ^{18}F-FDG PET has been accepted as a standard method of imaging and approved for procedure reimbursement. Increased uptake of ^{18}F-FDG in many types of tumors is due to the so-called Warburg effect [5], resulting from the oncogenic signaling-induced shift of tumor metabolism toward anaerobic glycolysis even under normoxic conditions [6, 7].

However, several tumor types do not accumulate ^{18}F-FDG at higher levels than the surrounding normal tissues, which makes the application of ^{18}F-FDG PET imaging for their diagnosis, staging, and monitoring of therapeutic interventions futile. Examples of such "^{18}F-FDG-nonavid" tumor types include prostate carcinoma [8], renal cell carcinoma [9, 10], hepatocellular carcinoma [11], and gastric cancers [12]. Furthermore, diagnostic PET imaging of some ^{18}F-FDG-avid tumors can be challenging because of their locations in tissues (organs) having high intrinsic glycolytic activity, such as brain gliomas [13]. ^{18}F-FDG-nonavid tumors represent a large fraction of malignancies for which the development and clinical translation of alternative PET imaging agents is urgently needed [14].

One such alternative agent is ^{11}C-labeled acetate (^{11}C-ACE). In the past two decades, ^{11}C-ACE has been used mainly to study myocardial metabolism [15–18]. In this application, the correlation of tracer washout from the myocardium to the rate of myocardial oxygen consumption has been established. It was shown that ^{11}C-CO_2 is the main radiolabeled metabolite of ^{11}C-ACE leaving the myocardium, indicating clearly that the tricarboxylic acid cycle (TCA) in myocardium is the main metabolic pathway of ^{11}C-ACE. More recently, ^{11}C-ACE has been evaluated in prostate cancer for differential diagnosis, staging, and follow-up of its recurrence after surgery or treatment [19–24]. Upon uptake into the cells by the mono-carboxylate transporter, the ^{11}C-ACE is utilized in multiple metabolic pathways including TCA, for generation of energy and for de novo fatty acid synthesis catalyzed by fatty acid synthase (FAS). FAS has a very low expression and activity in normal cells, but it is upregulated in many cancer types, including prostate, breast, and ovary. Such differential FAS over-expression and upregulation of lipogeneic activity in malignant cells as compared to normal cells is believed to be the mechanism for entrapment of ^{11}C-ACE-derived radioactivity in cancer cells, thereby enabling the detection of tumors with PET. However, the clinical utilization of ^{11}C-ACE is not widespread because of the relatively short physical half-life of ^{11}C ($t_{1/2}$=20.5 min), which precludes commercial

distribution and dictates the need for an on-site cyclotron and radiochemistry facility. Therefore, we and others have been developing and validating an ^{18}F-labeled analog of acetate, ^{18}F-fluoroacetate (^{18}F-FACE), as a clinically useful PET imaging agent. Compared to ^{11}C, the much longer half-life of ^{18}F ($t_{1/2}$=110 min) should offer not only a more manageable manufacturing and delivery process for ^{18}F-FACE but also the advantage of delayed imaging, with the potential for greater tumor-to-background ratios.

To date, there has been only one clinical case report in the literature regarding the potential efficacy of ^{18}F-FACE for the detection of primary prostate carcinoma and pelvic lymph node metastases [25]. Recently, Ponde *et al*. reported a study of PET imaging with ^{18}F-FACE in CWR22 tumor-bearing nu/nu mice and whole-body PET of a baboon [26]. The biodistribution, metabolism, and radiation dosimetry data obtained in rodents are not directly translatable into humans because the murine catabolism of ^{18}F-FACE to ^{18}F-fluoride greatly exceeds that in human beings. Therefore, in the same study, ^{18}F-FACE PET imaging of a single baboon was performed for an initial assessment of the biodistribution of ^{18}F-FACE at 1 and 2 h after intravenous injection of this radiotracer in a primate. In the baboon, almost no defluorination of ^{18}F-FACE was apparent, as evidenced by the lack of discernible radioactivity uptake in the skeletal structures. This limited study did not include dynamic PET imaging to obtain time–activity profiles of ^{18}F-FACE in different organs and tissues of the baboon or an analysis of radiolabeled metabolites in plasma and urine. It did not estimate the radiation dosimetry for human patients, which is necessary for translation of ^{18}F-FACE into the clinic.

In another recent study, Lindhe *et al*. [27] have performed a head-to-head comparison of the biodistribution, metabolism, and excretion of ^{11}C-ACE and ^{18}F-FACE in three cynomolgus monkeys and one domestic pig. The ^{11}C-ACE pharmacokinetics and organ distribution in both species were similar to those previously established in man. In contrast to ^{11}C-ACE, ^{18}F-FACE exhibited prolonged blood retention, no detectable trapping in the myocardium or salivary glands, rapid clearance from the liver, and extensive excretion to the bile and urine. Massive defluorination was seen in the pig, resulting in intense skeletal activity.

To facilitate translation of ^{18}F-FACE into the clinic and in preparation to a phase I clinical study, we have conducted studies aimed at assessing the pharmacokinetics, biodistribution, metabolism, radiation dosimetry, and acute toxicity of diagnostic dosages of ^{18}F-FACE in rhesus macaques. We demonstrate that diagnostic dosages of ^{18}F-FACE for PET imaging studies are similar to other ^{18}F-labeled agents.

Materials and Methods

Radiosynthesis of ^{18}F-Fluoroacetate

A simple, fully automated method was developed for the synthesis of no carrier added sodium ^{18}F-FACE (Fig. 1). This method of ^{18}F-FACE radiosynthesis differs in some of its steps from the previously reported radiosynthesis methods [26, 28–30].

Prior to each synthesis, all reagent reservoirs and transfer lines in the automated box were rinsed either with acetonitrile or sterile water for injection. A new set of disposable glass reactors, crimp top septa, and sterile needles were used for each synthesis. ^{18}F-fluoride was produced by irradiating ^{18}O-water (97%+ enrichment) with 18 MeV protons from a TR19/9 cyclotron (Advanced Cyclotron Systems, Richmond, BC, Canada). The irradiated ^{18}O-water was transferred through a Chromafix 30-PS-HCO_3 (Macherey-Nagel, Germany) ion exchange cartridge. ^{18}F was trapped with the Chromafix 30-PS-HCO_3 resin and then eluted

using standard K_2CO_3/Kryptofix$_{222}$ in an acetonitrile/water solution. Solvents were removed during the two-step evaporation processes that rendered the dried ^{18}F.

The precursor, ethyl (*p*-tosyloxy) acetate (ETA), was purchased from ABX (Radeberg, Germany), dissolved in 0.3 mL acetonitrile and added to the dry ^{18}F mixture. The reaction mixture was heated to 80°C and purged with a stream of nitrogen gas. The ^{18}F-EFACE and acetonitrile solvent were evaporated from the reaction mixture under the stated conditions and were trapped by a second vessel which contained 0.3 mL of 0.1 M sodium hydroxide maintained at 15°C. Evaporation of acetonitrile and simultaneous hydrolysis of ^{18}F-EFACE were completed within 5 min. The crude ^{18}F-FACE product was then passed through a preconditioned ion exchange resin AG1-X8 (BioRad, Hercules, CA, USA). The resin with the trapped product was rinsed three times with sterile water for injection that was sent to waste. Saline solution for injection (0.9% sodium chloride USP) was then used to elute ^{18}F-FACE. Hydrochloric acid (0.01 N) was added to bring the final pH of the product into the range of pH 6–8. The final product was analyzed using an HPLC model 1,100 (Agilent, Santa Clara, CA, USA) coupled to a UV–visible spectrum detector and a radioactivity detector Flowcount (Bioscan Inc., Washington, DC, USA), with a Supelcogel C-610H column (30 cm long; 7.8 mm internal diameter; Sigma-Aldrich, St. Louis, MO, USA) using 20 mM phosphoric acid aqueous solution as a mobile phase at a flow rate of 0.5 mL/min.

The final product was passed through a 0.22-μm sterile filter (Millipore) into a 30-mL sterile vial. A bubble point procedure was performed on the final filter to test filter integrity. Sterility was verified post hoc by incubation in soybean–casein digest medium for 14 days at 20–25°C. Pyrogenicity was determined by a Limulus amoebocyte lysate test using Endosafe®-PTS system (Charles River, Wilmington, MA, USA).

Determination of Specific Activity

Specific activity of ^{18}F-FACE was calculated based on measurements of radioactivity concentration and molar concentration in the dosing injectate. The radioactivity concentration of ^{18}F-FACE was determined using gamma spectrometer Packard 5500 gamma spectrometer (Perkin-Elmer, Waltham, MA, USA). The molar concentration of ^{18}F-FACE was determined using ion chromatography system ICS-2000 (Dionex, Sunnyvale, CA, USA) with potassium hydroxide eluent generator and IonPac AS11-HC, 4× 250 mm column (Dionex) maintained at 30°C; the potassium hydroxide mobile phase gradient was as follows: 0–8 min 1 mM/L, 8–18 min 1–15 mM/L, 18–28 min 15–45 mM/L, and 28–30 min 45 mM/L. To measure the concentration and total amount of fluoroacetate in the dosing injectate, a standard curve was established (linear fit R^2=0.9998) using authentic fluoroacetate standard (product number 31220; Sigma-Aldrich, St. Louis, MO, USA) at different concentrations ranging from 0.0241 to 24.1 μg/mL (0.0309 to 3.09 μM/L).

Experimental Animals

Six rhesus macaques (three female and three male animals) were included in this study (Table 1). The animals were housed separately in a facility accredited by the Association for Assessment and Accreditation of Laboratory Animal Care International, at The University of Texas MD Anderson Cancer Center. All experiments were performed following MD Anderson guidelines for conducting experiments in non-human primates under an Institutional Animal Care and Use Committee approved research protocol. Prior to imaging, the animals were fasted overnight but had free access to water. To facilitate the intubation of the trachea, the animals were pre-medicated with atropine sulfate 0.04 mg/kg intramuscularly (i.m.) and anesthetized with 2.2–4.4 mg/kg telazole i.m., or 10– 25 mg/kg ketamine i.m., followed by inhalation anesthesia with isoflurane 1.0–3.0% in oxygen and maintained by mechanical ventilation using an Ohmeda Excel 210 SE (Soma Technology,

Bloomfield, CT, USA). After intubation and stabilization of vital signs under anesthesia, the animals were cannulated in both saphenous veins: One cannula was used for injection of ^{18}F- FACE, and the other was used for repetitive blood sampling during imaging. Also, the urinary bladder was catheterized for collection of radioactive urine during PET/CT imaging. Body temperature was maintained at 37±0.8°C using an air-circulating heating device Model 505 (Arizant Healthcare, Praire, MN, USA). The electrocardiogram (ECG), blood pressure, pulse oxymetry, and respiration rates were monitored using a Solar 8000 system (Marquette Medical Systems, Milwaukee, WI, USA) throughout the imaging study.

PET Imaging Protocol

PET images were acquired using an ECAT HR+ (Siemens Molecular Imaging, Knoxville, TN, USA). After a 10-min transmission scan, 165.4±28.5 MBq (21.8±5.9 MBq/kg) of ^{18}F-FACE in a volume of 5 mL was administered intravenously over 2 min by a digital syringe pump (Harvard Apparatus, Holliston, MA, USA). After injection of the radiotracer, a total of 29 frames were acquired in the first 30 min with 2D mode acquisition (20 frames for 15 s each, 5 frames for 1 min each, and 4 frames for 5 min each) in the area from the lower thorax to the upper abdomen. This enabled the acquisition of time–activity curves for the lungs, heart, aorta (blood), liver, mediastinal structure, stomach, and upper tips of the kidneys during the first half-hour following administration. Thereafter, three consecutive whole-body static scans were performed with the following protocol: Transmission and emission scans were 3 and 5 min, respectively, for four to five bed positions with acquisition in a 2D mode. PET images were reconstructed using standard vendor-provided reconstruction algorithms, which incorporated ordered-subset expectation maximization and corrected for attenuation; the emission data were corrected for scatter, random events, and dead-time losses using the manufacturer's software program. To ensure that the injected dosage was accurate in terms of measured activity using PET, a CRC-15R dose calibrator (Capintec, Pittsburgh, PA, USA) was cross-calibrated with the PET instrument.

CT Study

A CT examination was performed using either a HiSpeed Advantage or a Light Speed 4-Slice helical CT scanner (GE Healthcare, Milwaukee, WI, USA) on the same day that the PET study was performed. The axial images were converted to Digital Imaging and Communications in Medicine Digital Imaging and Communications in Medicine (DICOM) image files for registration with the PET images.

Image Analysis

Regional dynamic and whole-body reconstructed PET and CT data were stored in the DICOM file format. Three-dimensional volumes of interest (VOIs) of individual source organs were constructed on the PET images to include all organ activity. These VOIs were used for PET image analysis. The following source organs were analyzed: the heart, liver, gallbladder, kidneys, urinary bladder, intestines, and whole body. Three-dimensional VOI definitions were used to visually inspect for movement artifacts between sequential scans in the same segment. Residual errors were manually corrected by redefining VOIs when necessary.

Time-Integrated Activity Coefficient and Absorbed Radiation Dose Calculations

Individual organ time–activity curves were estimated by fitting volume of interest data from the whole-body scans to a mono-exponential function using the Sigma Plot software program (version 11; Systat Software, Chicago, IL, USA) for five of the six animals. Only two whole-body scans were acquired for the sixth animal and so the rate of clearance was estimated by a linear fit to the logarithms of the two measured points. The whole-body time–

activity curves were constructed by taking the activity in the entire animal (including the urinary bladder) in the first whole-body scan and decay-correcting it to the time of administration. This was assumed to represent the entirety of the administered activity. The second time point was constructed by taking the activity in the entire animal less that of the bladder at the time of the first whole-body scan. The remaining two time points, or in one case one time point, were constructed from the corresponding whole-body activity measurements less those of the urinary bladder. The time-integrated activity coefficient (formerly called the residence time [31]) was calculated by dividing the fractional uptake parameter of the exponential fit to the original data (not corrected for decay) by the decay constant of the fit.

The time-integrated activity coefficients were “humanized” using the mass of each of the identified source organs estimated from CT scans of the non-human primates and the masses of those organs tabulated by the OLINDA/EXM 1.1 (Vanderbilt University, Nashville, TN, USA) software for its 73.7-kg adult male model. The non-human primate and human organ masses were normalized by the respective whole-body masses, and each time-integrated activity coefficient was scaled by the ratio of the human to nonhuman normalized organ masses [32]. The human dosimetry of ^{18}F-FACE was then estimated using these humanized time-integrated activity coefficients and the adult male model in the OLINDA/EXM 1.1 software program.

Blood Sampling and Analyses

Immediately before ^{18}F-FACE injection in each animal, a 0.5-mL blood sample was drawn to measure the hematocrit and blood gases with an i-STAT portable analyzer (Abbott Point of Care, Princeton, NJ, USA). ^{18}F-FACE was injected only if the hematological and blood chemical parameters in the blood sample were all within the normal ranges. Subsequently, 0.5-mL venous blood samples were obtained via the catheterized vein at 10, 20, 40, 60, and 90 s and 2, 3, 5, 8, 16, 32, 60, 90, 120, and 180 min after ^{18}F-FACE injection. At the end of each PET/CT imaging session, an additional blood sample (0.5 mL) was obtained and analyzed using the i-STAT portable analyzer to determine potential acute toxic side effects from the diagnostic dosage of ^{18}F-FACE.

The total radioactivity in the blood and plasma compartments was assayed for radioactivity concentration using a gamma counter (Cobra Quantum, Perkin-Elmer, Waltham, MA, USA). A portion of each plasma sample was ultrafiltered with a Biomax filter (Millipore, Billerica, MA, USA) before it was analyzed by HPLC The chromatographic conditions were the same as described in the section on the HPLC analytical method. The elution times of ^{18}F-FACE and major potential radiolabeled metabolites in blood plasma (^{18}F-fluorocitrate and ^{18}F-fluoride) were determined using authentic cold standards under the same chromatographic conditions. Fractions of ^{18}F-FACE and ^{18}F-labeled metabolites were calculated for each sample based on the area under each peak. The total radioactivity in the plasma was expressed as %ID/mL and plotted against time post-injection of ^{18}F-FACE. Also, the %ID/mL of intact ^{18}F-FACE and ^{18}F-metabolites were calculated, based on the results of the radio-HPLC analyses and were plotted against time post-injection of ^{18}F-FACE to generate the corresponding time–activity curves.

Urine Analysis

Each animal’s urinary bladder was catheterized with a Foley catheter. The line was clamped until after the second whole-body image had been acquired. In five of the six animals, the line was then unclamped. At 120–150 min after administration of ^{18}F-FACE, the urine was collected (mean volume of 38±21 mL). The total radioactivity of each sample was measured

using a gamma counter. Samples were subjected to the same radio-HPLC analysis as described above for analysis of blood samples.

Results

^{18}F-FACE Synthesis

Using an automated synthesizer, we have obtained greater than 97% pure ^{18}F-FACE at a radioactivity yield greater than 50%. Analysis of the final product using HPLC showed a major peak eluting at the same retention time, 14.7 min, as the sodium fluoroacetate standard. A trace amount of ^{18}F-fluoride (<0.5%) eluting at 13.7 min in the product is also detected (Fig. 2). The product maintained its radiochemical purity for more than 8 h after the completion of the synthesis. Based on ion chromatography and radioactivity measurements, the specific activity of the synthesized ^{18}FFACE was 1.162 Ci/μM (43 GBq/μ,M). The total pharmacologic “cold” equivalent of fluoroacetate administered to the animals in a single dose of 165–200 MBq ^{18}F-FACE was 0.30–0.36 ng (or 1.815 pg/MBq).

PET Imaging of Pharmacokinetics and Biodistribution of ^{18}F-FACE

Dynamic PET imaging demonstrated that the hepatobiliary and renal systems were the principal pathways of clearance of ^{18}F-FACE (Fig. 3). A relatively low accumulation of ^{18}F-FACE-derived radioactivity was observed in the majority of organs not involved in biological clearance of ^{18}F-FACE-derived radioactivity. Some accumulation of ^{18}F-FACE was observed in the myocardium. No significant accumulation or retention of ^{18}F-FACE was observed in the brain. There was some low level deposition of radioactivity in the skeletal structures, predominantly in the shoulder and hip joints, indicating a gradual defluorination occurring over 2 to 3 h post-injection of the radiotracer. Consistent with this observation, an increased level of free ^{18}F-fluoride was detected in blood and urine samples collected at 2 to 3 h after the radiotracer administration.

The time-dependent dynamics of ^{18}F-FACE-derived radioactivity concentration in different organs and tissues were determined from PET images (Fig. 4a). Within 5 min, the level of radioactivity in the blood reached 0.040±0.02% ID/g and then cleared bi-exponentially with the fast phase between 3 and 18 min (half-life of 4 min) and then a slow phase until 180 min (half-life of 250 min). The fraction of ^{18}F-fluoride in the blood gradually increased over time, but it was still less than 9% of the whole blood radioactivity at 180 min after ^{18}F-FACE administration (Fig. 4b). The partition of radioactivity in the blood, 70% in the plasma and 30% in the red blood cells, was stable throughout the study (Fig. 5). Rapid accumulation of the radioactivity into the liver and kidney was observed, reaching concentrations of 0.040% ID/g (organ tissue) and 0.047% ID/g, respectively, at 5 min. There was a relatively low level of uptake in lung and muscle and other organs throughout the 180 min of the study; 27.6% of the total radioactivity in urine was determined to be ^{18}F-fluoride, while 72.4% was ^{18}F-FACE.

Evaluation of Acute Toxicity from ^{18}F-FACE

ECG traces after intravenously injection of [^{18}F]-FACE and quantitative measures of different intervals are summarized in Fig. 6 and Table 2. None of the animals injected with ^{18}F-FACE demonstrated any significant changes in cardiac rhythm or electrical activity patterns from the time of administration to 180 min post-injection. Hematologic parameters before and after the PET study with ^{18}F-FACE are summarized in Table 3. There were no statistically significant changes in blood chemistry, liver enzymes, or renal function before, after 3 h, and over a period of 1– 3 months after the tracer administration, demonstrating the absence of any acute or chronic toxicity attributable to ^{18}FFACE.

Radiation Dosimetry

To assess human radiation exposure due to diagnostic dosages of ^{18}F-FACE, the radiation absorbed doses to organs were estimated using organ time-integrated activity coefficients from each individual animal that were "humanized" (Table 4). These doses are expressed in millisieverts per megabecquerel (Table 5) because the radiation-weighting factor of the ionizing radiation arising from F-18 is included in the organ dose calculations that were performed using the OLINDA/EXM 1.1 software. The effective dose for the adult male dosimetric model was estimated to be 0.0211 mSv/MBq. The higher absorbed doses were estimated for the liver (0.0307 mSv/MBq), the gallbladder wall (0.0288 mSv/MBq), the intestines (0.0366–0.0745 mSv/MBq), and the kidneys (0.0342 mSv/MBq), while much lower radiation absorbed doses were estimated for the brain (0.00762 mSv/MBq), breast (0.00774 mSv/MBq), thyroid (0.00888 mSv/MBq), and red bone marrow (0.0102 mSv/MBq).

Discussion

This study was conducted to facilitate the clinical phase I study with ^{18}F-FACE, as an alternative to ^{11}C-ACE for imaging ^{18}F-FDG-nonavid tumors. Previously, ^{11}C-ACE PET was reported to be up to 100% effective for detection of primary tumors in patients with untreated prostate cancer, in contrast to other conventional imaging methods such as ^{18}F-FDG PET, and to have a 59% sensitivity for detection of recurrent prostate cancer in patients with prostate-specific antigen relapse [19, 20, 33]. The use of ^{18}F-FACE PET/CT has been reported in only one prostate cancer patient [25]. In the latter study, a dosage of 280 MBq ^{18}F-FACE was injected intravenously, and PET imaging was started 70 min after dosing. In that study, ^{18}F-FACE PET/CT images demonstrated moderate to intense uptake in several, but not all, of the metastatic lesions.

In this current study, the pattern of biodistribution and clearance of ^{18}F-FACE in rhesus macaques was similar to that reported before in a baboon [26] and in cynomologous monkeys [27]. The present work reports for the first time radiation dosimetry estimates made in non-human primates and scaled to human patients. Based on the results of the current studies in rhesus macaques, the estimated effective dose to human patients after administration of 185–370 MBq of ^{18}F-FACE is 3.90–7.81 mSv. This is consistent with the previously reported range of 5.7–7.0 mSv for 300–370 MBq [34] and 3.8–10.7 mSv for 185–370 MBq [35] of ^{18}F-FDG. The critical organs for ^{18}F-FACE were the intestines (0.0366–0.0745 mSv/MBq), which is due to combined radiation exposure from the surrounding organs such as the liver, kidney, and urinary bladder. For comparison, the reported radiation absorbed doses after administration of ^{11}C-ACE in humans were the highest in the pancreas (0.017 mGy/MBq), intestines (0.01–0.011 mGy/MBq), and kidneys (0.0093 mGy/MBq), followed by the liver and the urinary bladder with 0.006 and 0.0028 mGy/MBq, respectively. The effective dose was estimated to be 0.0049 mSv/MBq [36]. In contrast to the well-established hepatobiliary clearance of ^{11}C-ACE from the circulation, ^{18}F-FACE cleared predominantly through the kidneys into the urinary bladder, which corroborates previous reports [26, 27]. These results suggest that the diagnostic dosage of 370 MBq of ^{18}F-FACE should be acceptable for administration in human patients and that its effects are well below the limit of 50 mSv per organ per year, which is set forth in the FDA regulations (21 CFR 361.1) [32, 37, 38].

This study demonstrated that the uptake of ^{18}F-FACE-derived radioactivity in skeletal structures in monkeys was limited and that defluorination (measured in blood samples) was no more than 9% of the total at the end of the 3-h study and ^{18}F-fluorocitrate anabolite was not detectable. Our results are in agreement with those reported previously in non-human primates, where only a minimal level of bone uptake of ^{18}F-FACE-derived radioactivity was

observed [26, 27]. In contrast, defluorination of ^{18}F-FACE in rodents has been significant [39], and large amounts of ^{18}F-fluoride liberated from ^{18}F-FACE accumulate in rodent skeletal structures [26]. The high expression of glutathione S-transferase in rats and mice is responsible for the observed defluorination of fluoroacetate [40], which makes it a suboptimal radiotracer for PET imaging studies in rodents. Nevertheless, recent studies by Marik *et al*. [41] demonstrated the potential utility of ^{18}F-FACE for imaging of glial activation in a murine model of intracerebral glioma, stroke, and cerebral ischemia–hypoxia. In contrast, Lindhe *et al*. [27] drew the paradoxical conclusion that ^{18}F-FACE could not be regarded as a functional analog of ^{11}C-ACE and that it is of little use for studies of organ blood flow, intermediary metabolism, or lipid synthesis. Therefore, the mechanism of ^{18}F-FACE uptake and accumulation in tumor cells requires additional discussion.

The biochemical perspectives of PET imaging with ^{11}C-ACE have been discussed recently in the literature [24]. The mechanism of ^{18}F-FACE uptake and accumulation in cells is similar to that of ^{11}C-ACE. Fluoroacetate is transported through cell membranes by a monocarboxylate transporter or by diffusion and is subsequently converted to fluoroacetyl-CoA by the enzyme acetyl-CoA synthases 1 and 2 (ACS1, ACS2) [42, 43]. At least three main metabolic pathways can utilize the ^{18}F-fluoroacetyl-CoA. One is the TCA cycle [44, 45]. However, unlike acetate, fluoroacetate stops the TCA cycle from its completion after the formation of fluorocitrate. Fluorocitrate acts as an irreversible inhibitor of aconitase [46], which is the catalytic enzyme for the conversion of citrate to *cis*-citrate, a necessary intermediate for the successful completion of the TCA cycle. Hence, ^{18}F-fluorocitrate is accumulated in cells until it degrades radiochemically. While citrate can be utilized by the ATP citrate lyase, which is one of the key lipogeneic enzymes that is over-expressed in many cancer cells [47], fluorocitrate cannot be utilized by ATP citrate lyase because it is irreversibly bound to aconitase. Another metabolic pathway of acetyl-CoA utilization is fatty acid synthesis catalyzed by the enzyme FAS, which is upregulated in many types of cancer cells [47]. However, fluoroacetyl-CoA is not an efficient substrate for FAS, and therefore, the fluoroacetyl moiety is not incorporated into the de novo synthesized fatty acids. Nevertheless, the expression and activity of acetyl-coA synthase is proportionally upregulated in tumor cells either with high glycolytic activity (TCA cycle) or high FAS activity, such as in prostate carcinoma cells, which mediates formation and accumulation of ^{18}F-fluoroacetyl-CoA and may explain increased uptake and accumulation of ^{18}F-FACE.

The third metabolic pathway that may utilize acetyl-coA is ketone body synthesis through formation of acetoacetate mediated by the cooperative action of acetyl-CoA transferase and acetoacetyl-CoA thiolase followed by succinyl coenzyme A/acetoacetate coenzyme transferase, an initiator of ketone body utilization in tumor cells [48, 49]. Therefore, it is conceivable that fluoroacetate in tracer dosages may be converted in part to fluoroacetoacetate, which would reflect de novo ketone synthetic activity in cancer cells, which utilize ketone bodies for energy production. Thus, there is plenty of evidence that ^{18}F-FACE can be used for metabolic studies and imaging tumors with upregulated glycolysis, fatty acid synthesis, and ketone metabolism.

Although ^{18}F-FACE may be a promising PET radiotracer, there have been concerns raised about potential toxicity of this compound in tracer dosages, which may have hindered its clinical translation. The data obtained from our studies and those of the others put these concerns in perspective. Fluoroacetate is a naturally occurring substance that can be found in the leaves of *Dichapetalum cymosum*, a poisonous South African plant, and in 40 other plant species including tea leaves. For the past half-century, chemically synthesized sodium fluoroacetate has been used as a vertebrate poison to help control opossum overpopulation in New Zealand. In the USA, sodium fluoroacetate is used in collars worn by livestock to protect them from aggressive predators. The pharmacology and toxicology of sodium

fluoroacetate have been studied extensively in many animal species including rodents, dogs [50, 51], various livestock, and monkeys and have been recently reviewed [52]. The LD_{50} for dog is 60 μg/kg if administered intravenously and 66 μg/kg if administered orally. The LD_{50} for monkey is 5 and 300 mg/kg through intravenous injection and oral consumption, respectively. The estimated lethal dose for human is approximately 2–10 mg/kg [53–55]. Tea leaves are found to contain fluoroacetate at 0.19 μg/g of leaves [56]. If 3–6 g of tea leaves is commonly used to make a cup of tea, they could release fluoroacetate in the range of 0.57 to 1.14 μg. The anticipated initial dosage of 260 MBq of ^{18}F-FACE for PET imaging in a phase I study equates to a pharmacologic mass dose of 0.47 ng, determined based on our measurements of specific activity of ^{18}F-FACE (43 GBq/μ,M). For comparison, a cup of tea may contain approximately 1,000– 2,500 times more fluoroacetate than that in one diagnostic administration of ^{18}F-FACE. It is well established that fluoroacetate toxicity is due to biosynthesis of fluorocitrate, which blocks the TCA cycle and causes cell death [57]. The fluorocitrate inhibition of aconitase and citrate transporters has been studied extensively [46, 58–61]. Within 1 h, the level of citrate in many organs increases more than tenfold. Citrate buildup further inhibits glucose metabolism by inhibiting the enzyme phosphofructokinase, which causes toxicity. However, at tracer doses administered to humans (i.e., <1 ng total dose), ^{18}F-FACE cannot elicit any pharmacological or toxic effects. Furthermore, unlike “cold” (non-radiofluorinated) fluoroacetate, which contains a stable isotope of fluorine, in ^{18}F-FACE the ^{18}F radionuclide decays to ^{18}O, resulting in a molecule that is no longer fluoroacetate and which dissociates from aconitase and citrate transporters, thus restoring the normal activity of TCA cycle.

Finally, in the current study, no significant changes to the ECG were observed during imaging studies, which indicates that there was no acute myocardial toxicity from the injection of ^{18}F-FACE in rhesus macaques. Follow-up examinations immediately after PET imaging with ^{18}F-FACE as well as 1– 3 month later revealed no significant changes in CBC, liver enzymes, or renal function when compared to data obtained prior to this radiotracer administration. Therefore, based on volumes of well-established toxicology of fluoroacetate in various species together with results of the current study in rhesus macaques, we are confident that it is pharmacologically safe to employ ^{18}F-FACE as a PET tracer for human use at the proposed diagnostic doses.

Conclusions

The pharmacokinetics, metabolism, biodistribution, radiation dosimetry characteristics, and lack of acute and delayed toxicity of ^{18}F-FACE determined in non-human primates indicate that diagnostic doses of this radiotracer are similar to those of other agents used for PET imaging in human patients. The highest radiation dose is delivered to the intestines. This dose estimation, as well as the radiation doses delivered to other radiosensitive organs, must be considered in evaluating the dosimetry of multiple administration of ^{18}F-FACE to human patients.

Acknowledgments

This work was supported by the NIH-NCI CA-016672 (MD Anderson Cancer Center Support Grant) and new project development funds of the Department of Experimental Diagnostic Imaging, MDACC. We thank Nancy Swanston, CNMT, for help with the PET studies, Karen Yoas for help in coordinating this study, and the anonymous reviewers for their insights and advice.

References

1. Hustinx R, Benard F, Alavi A. Whole-body FDG-PET imaging in the management of patients with cancer. Semin Nucl Med. 2002; 32:35–46. [PubMed: 11839068]

2. Kelloff GJ, Hoffman JM, Johnson B, Scher HI, Siegel BA, Cheng EY, Cheson BD, O'Shaughnessy J, Guyton KZ, Mankoff DA, Shankar L, Larson SM, Sigman CC, Schilsky RL, Sullivan DC. Progress and promise of FDG-PET imaging for cancer patient management and oncologic drug development. Clin Cancer Res. 2005; 11:2785–2808. [PubMed: 15837727]
3. Ide M. Cancer screening with FDG-PET. Q J Nucl Med Mol Imaging. 2006; 50:23–27. [PubMed: 16557201]
4. Wahl RL, Jacene H, Kasamon Y, Lodge MA. From RECIST to PERCIST: evolving considerations for PET response criteria in solid tumors. J Nucl Med. 2009; 50(Suppl 1):122S–150S. [PubMed: 19403881]
5. Warburg O. On the origin of cancer cells. Science. 1956; 123:309–314. [PubMed: 13298683]
6. Busk M, Horsman MR, Jakobsen S, Bussink J, van der Kogel A, Overgaard J. Cellular uptake of PET tracers of glucose metabolism and hypoxia and their linkage. Eur J Nucl Med Mol Imaging. 2008; 35:2294–2303. [PubMed: 18682937]
7. Busk M, Horsman MR, Kristjansen PE, van der Kogel AJ, Bussink J, Overgaard J. Aerobic glycolysis in cancers: implications for the usability of oxygen-responsive genes and fluorodeoxyglucose-PET as markers of tissue hypoxia. Int J Cancer. 2008; 122:2726–2734. [PubMed: 18351643]
8. Bouchelouche K, Oehr P. Recent developments in urologic oncology: positron emission tomography molecular imaging. Curr Opin Oncol. 2008; 20:321–326. [PubMed: 18391633]
9. Kumar R, Zhuang H, Alavi A. PET in the management of urologic malignancies. Radiol Clin North Am. 2004; 42:1141–1153. ix. [PubMed: 15488563]
10. Lawrentschuk N, Davis ID, Bolton DM, Scott AM. Functional imaging of renal cell carcinoma. Nat Rev Urol. 2010; 7:258–266. [PubMed: 20448659]
11. Wolfort RM, Papillion PW, Turnage RH, Lillien DL, Ramaswamy MR, Zibari GB. Role of FDG-PET in the evaluation and staging of hepatocellular carcinoma with comparison of tumor size, AFP level, and histologic grade. Int Surg. 2011; 95:67–75. [PubMed: 20480845]
12. Ott K, Herrmann K, Krause BJ, Lordick F. The value of PET imaging in patients with localized gastroesophageal cancer. Gastrointest Cancer Res. 2008; 2:287–294. [PubMed: 19259277]
13. Lau EW, Drummond KJ, Ware RE, Drummond E, Hogg A, Ryan G, Grigg A, Callahan J, Hicks RJ. Comparative PET study using F-18 FET and F-18 FDG for the evaluation of patients with suspected brain tumour. J Clin Neurosci. 2011; 17:43–49. [PubMed: 20004582]
14. Nanni C, Fantini L, Nicolini S, Fanti S. Non FDG PET. Clin Radiol. 2010; 65:536–548. [PubMed: 20541653]
15. Pike VW, Eakins MN, Allan RM, Selwyn AP. Preparation of [1–11C]acetate—an agent for the study of myocardial metabolism by positron emission tomography. Int J Appl Radiat Isot. 1982; 33:505–512. [PubMed: 6981606]
16. Schelbert HR. PET contributions to understanding normal and abnormal cardiac perfusion and metabolism. Ann Biomed Eng. 2000; 28:922–929. [PubMed: 11144676]
17. Timmer SA, Germans T, Gotte MJ, Russel IK, Dijkmans PA, Lubberink M, ten Berg JM, ten Cate FJ, Lammertsma AA, Knaapen P, van Rossum AC. Determinants of myocardial energetics and efficiency in symptomatic hypertrophic cardiomyopathy. Eur J Nucl Med Mol Imaging. 2010; 37:779–788. [PubMed: 20069294]
18. Timmer SA, Lubberink M, Germans T, Gotte MJ, ten Berg JM, ten Cate FJ, van Rossum AC, Lammertsma AA, Knaapen P. Potential of [^{11}C] acetate for measuring myocardial blood flow: studies in normal subjects and patients with hypertrophic cardiomyopathy. J Nucl Cardiol. 2010; 17:264–275. [PubMed: 20039151]
19. Oyama N, Akino H, Kanamaru H, Suzuki Y, Muramoto S, Yonekura Y, Sadato N, Yamamoto K, Okada K. ^{11}C-acetate PET imaging of prostate cancer. J Nucl Med. 2002; 43:181–186. [PubMed: 11850482]
20. Oyama N, Miller TR, Dehdashti F, Siegel BA, Fischer KC, Michalski JM, Kibel AS, Andriole GL, Picus J, Welch MJ. ^{11}C-acetate PET imaging of prostate cancer: detection of recurrent disease at PSA relapse. J Nucl Med. 2003; 44:549–555. [PubMed: 12679398]

21. Kotzerke J, Volkmer BG, Neumaier B, Gschwend JE, Hautmann RE, Reske SN. Carbon-11 acetate positron emission tomography can detect local recurrence of prostate cancer. Eur J Nucl Med Mol Imaging. 2002; 29:1380–1384. [PubMed: 12271422]
22. Fricke E, Machtens S, Hofmann M, van den Hoff J, Bergh S, Brunkhorst T, Meyer GJ, Karstens JH, Knapp WH, Boerner AR. Positron emission tomography with ^{11}C-acetate and ^{18}F-FDG in prostate cancer patients. Eur J Nucl Med Mol Imaging. 2003; 30:607–611. [PubMed: 12589476]
23. Sandblom G, Sorensen J, Lundin N, Haggman M, Malmstrom PU. Positron emission tomography with C11-acetate for tumor detection and localization in patients with prostate-specific antigen relapse after radical prostatectomy. Urology. 2006; 67:996–1000. [PubMed: 16698359]
24. Soloviev D, Fini A, Chierichetti F, Al-Nahhas A, Rubello D. PET imaging with ^{11}C-acetate in prostate cancer: a biochemical, radiochemical and clinical perspective. Eur J Nucl Med Mol Imaging. 2008; 35:942–949. [PubMed: 18338167]
25. Matthies A, Ezziddin S, Ulrich EM, Palmedo H, Biersack HJ, Bender H, Guhlke S. Imaging of prostate cancer metastases with ^{18}F-fluoroacetate using PET/CT. Eur J Nucl Med Mol Imaging. 2004; 31:797. [PubMed: 14985862]
26. Ponde DE, Dence CS, Oyama N, Kim J, Tai YC, Laforest R, Siegel BA, Welch MJ. 18F–fluoroacetate: a potential acetate analog for prostate tumor imaging—*in vivo* evaluation of 18F–fluoroacetate *versus* 11C–acetate. J Nucl Med. 2007; 48:420–428. [PubMed: 17332620]
27. Lindhe O, Sun A, Ulin J, Rahman O, Langstrom B, Sorensen J. [^{18}F] Fluoroacetate is not a functional analogue of [^{11}C]acetate in normal physiology. Eur J Nucl Med Mol Imaging. 2009; 36:1453–1459. [PubMed: 19387639]
28. Sykes TR, Ruth TJ, Adam MJ. Synthesis and murine tissue uptake of sodium [^{18}F]fluoroacetate. Int J Radiat Appl Instrum B. 1986; 13:497–500.
29. Jeong JMLD, Chung J-K, Lee MC, Koh C-S, Kang SS. Synthesis of no-carrier-added [^{18}F]fluoroacetate. J Labelled Compd Radiopharm. 1997; 39:395–399.
30. Sun LQ, Mori T, Dence CS, Ponde DE, Welch MJ, Furukawa T, Yonekura Y, Fujibayashi Y. New approach to fully automated synthesis of sodium [18 F]fluoroacetate—a simple and fast method using a commercial synthesizer. Nucl Med Biol. 2006; 33:153–158. [PubMed: 16459271]
31. Bolch WE, Eckerman KF, Sgouros G, Thomas SR. MIRD pamphlet no. 21: a generalized schema for radiopharmaceutical dosimetry-standardization of nomenclature. J Nucl Med. 2009; 50:477–484. [PubMed: 19258258]
32. Macey, DJWL.; Breitz, HB.; Liu, A.; Johnson, TK.; Zanzonico, PB. A primer for radioimmunotherapy and radionuclide therapy. AAPM report no 7. 2001. http://www.aapm.org/pubs/reports/rpt_71.pdf
33. Morris MJ, Scher HI. ^{11}C-acetate PET imaging in prostate cancer. Eur J Nucl Med Mol Imaging. 2007; 34:181–184. [PubMed: 17238014]
34. Brix G, Lechel U, Glatting G, Ziegler SI, Munzing W, Muller SP, Beyer T. Radiation exposure of patients undergoing whole-body dual-modality ^{18}F-FDG PET/CT examinations. J Nucl Med. 2005; 46:608–613. [PubMed: 15809483]
35. Deloar HM, Fujiwara T, Shidahara M, Nakamura T, Watabe H, Narita Y, Itoh M, Miyake M, Watanuki S. Estimation of absorbed dose for 2-[F-18]fluoro-2-deoxy-D-glucose using whole-body positron emission tomography and magnetic resonance imaging. Eur J Nucl Med. 1998; 25:565–574. [PubMed: 9618570]
36. Seltzer MA, Jahan SA, Sparks R, Stout DB, Satyamurthy N, Dahlbom M, Phelps ME, Barrio JR. Radiation dose estimates in humans for ^{11}C-acetate whole-body PET. J Nucl Med. 2004; 45:1233–1236. [PubMed: 15235071]
37. Anonymous. Radiation dose to patients from radiopharmaceuticals (addendum 2 to ICRP publication 53). Ann ICRP. 1998; 28:1–126.
38. Kase KR. Radiation protection principles of NCRP. Health Phys. 2004; 87:251–257. [PubMed: 15303061]
39. Liu RS, Chou TK, Chang CH, Wu CY, Chang CW, Chang TJ, Wang SJ, Lin WJ, Wang HE. Biodistribution, pharmacokinetics and PET imaging of [(18)F]FMISO, [^{18}F]FDG and [^{18}F]FAc in a sarcoma-and inflammation-bearing mouse model. Nucl Med Biol. 2009; 36:305–312. [PubMed: 19324276]

40. Tecle B, Casida JE. Enzymatic defluorination and metabolism of fluoroacetate, fluoroacetamide, fluoroethanol, and (−)-erythro-fluorocitrate in rats and mice examined by ^{19}F and ^{13}C NMR. Chem Res Toxicol. 1989; 2:429–435. [PubMed: 2519733]
41. Marik J, Ogasawara A, Martin-McNulty B, Ross J, Flores JE, Gill HS, Tinianow JN, Vanderbilt AN, Nishimura M, Peale F, Pastuskovas C, Greve JM, van Bruggen N, Williams SP. PET of glial metabolism using 2-^{18}F-fluoroacetate. J Nucl Med. 2009; 50:982–990. [PubMed: 19443600]
42. Muir D, Berl S, Clarke DD. Acetate and fluoroacetate as possible markers for glial metabolism *in vivo* . Brain Res. 1986; 380:336–340. [PubMed: 3756485]
43. Clarke DD. Fluoroacetate and fluorocitrate: mechanism of action. Neurochem Res. 1991; 16:1055–1058. [PubMed: 1784332]
44. Peters R, Wakelin RW. Biochemistry of fluoroacetate poisoning; the isolation and some properties of the fluorotricarboxylic acid inhibitor of citrate metabolism. Proc R Soc Lond B Biol Sci. 1953; 140:497–507. [PubMed: 13027279]
45. Proudfoot AT, Bradberry SM, Vale JA. Sodium fluoroacetate poisoning. Toxicol Rev. 2006; 25:213–219. [PubMed: 17288493]
46. Lauble H, Kennedy MC, Emptage MH, Beinert H, Stout CD. The reaction of fluorocitrate with aconitase and the crystal structure of the enzyme-inhibitor complex. Proc Natl Acad Sci USA. 1996; 93:13699–13703. [PubMed: 8942997]
47. Menendez JA, Lupu R. Fatty acid synthase and the lipogenic phenotype in cancer pathogenesis. Nat Rev Cancer. 2007; 7:763–777. [PubMed: 17882277]
48. Lopes-Cardozo M, Mulder I, van Vugt F, Hermans PG, van den Bergh SG, Klazinga W, de Vries-Akkerman E. Aspects of ketogenesis: control and mechanism of ketone-body formation in isolated rat-liver mitochondria. Mol Cell Biochem. 1975; 9:155–173. [PubMed: 1196305]
49. Fenselau A, Wallis K, Morris HP. Subcellular localization of acetoacetate coenzyme A transferase in rat hepatomas. Cancer Res. 1976; 36:4429–4433. [PubMed: 187322]
50. Yamashita K, Yada H, Ariyoshi T. Neurotoxic effects of alpha-fluoro-beta-alanine (FBAL) and fluoroacetic acid (FA) on dogs. J Toxicol Sci. 2004; 29:155–166. [PubMed: 15206584]
51. Goh CS, Hodgson DR, Fearnside SM, Heller J, Malikides N. Sodium monofluoroacetate (compound 1080) poisoning in dogs. Aust Vet J. 2005; 83:474–479. [PubMed: 16119418]
52. Goncharov NV, Jenkins RO, Radilov AS. Toxicology of fluoroacetate: a review, with possible directions for therapy research. J Appl Toxicol. 2006; 26:148–161. [PubMed: 16252258]
53. Gajdusek DC, Luther G. Fluoroacetate poisoning a review and report of a case. Am J Dis Child. 1950; 79:310–320. [PubMed: 15405402]
54. Harrisson JW, Ambrus JL, Ambrus CM. Fluoroacetate 1080 poisoning. Ind Med Surg. 1952; 21:440–442. [PubMed: 12999329]
55. Harrisson JW, Ambrus JL, Ambrus CM, Rees EW, Peters RH Jr, Reese LC. Acute poisoning with sodium fluoroacetate (compound 1080). J Am Med Assoc. 1952; 149:1520–1522. [PubMed: 14945963]
56. Vartiainen T, Gynther J. Fluoroacetic acid in guar gum. Food Chem Toxicol. 1984; 22:307–308. [PubMed: 6539279]
57. Savarie, P. Toxic characteristics of fluorocitrate, the toxic metabolite of compound 1080. 11th Vertebrate Pest Conference University of Nebraska, Lincoln, University of Nebraska; Lincoln. 1984. p. 132-137.
58. Carrell HL, Glusker JP, Villafranca JJ, Mildvan AS, Dummel RJ, Kun E. Fluorocitrate inhibition of aconitase: relative configuration of inhibitory isomer by x-ray crystallography. Science. 1970; 170:1412–1414. [PubMed: 5481856]
59. Villafranca JJ, Platus E. Fluorocitrate inhibition of aconitase. Reversibility of the inactivation. Biochem Biophys Res Commun. 1973; 55:1197–1207. [PubMed: 4771993]
60. Brand MD, Evans SM, Mendes-Mourao J, Chappell JB. Fluorocitrate inhibition of aconitate hydratase and the tricarboxylate carrier of rat liver mitochondria. Biochem J. 1973; 134:217–224. [PubMed: 4723224]
61. Eanes RZ, Kun E. Inhibition of liver aconitase isozymes by (−)-erythro-fluorocitrate. Mol Pharmacol. 1974; 10:130–139. [PubMed: 4846186]

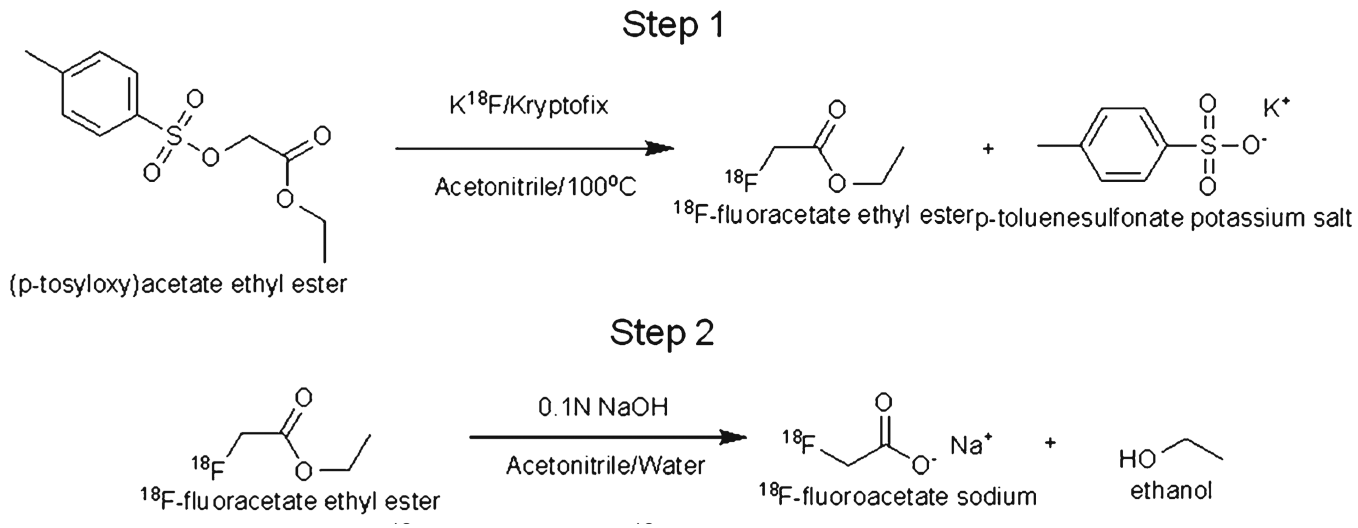

Fig. 1.

Scheme for radiosynthesis of ^{18}F-Fluoroacetate (^{18}F-FACE). *Step 1*: radiolabel ETA to form the intermediate, ^{18}F-fluoroacetate ethyl ester. *Step 2*: hydrolysis of EFA to form sodium ^{18}F-FACE.

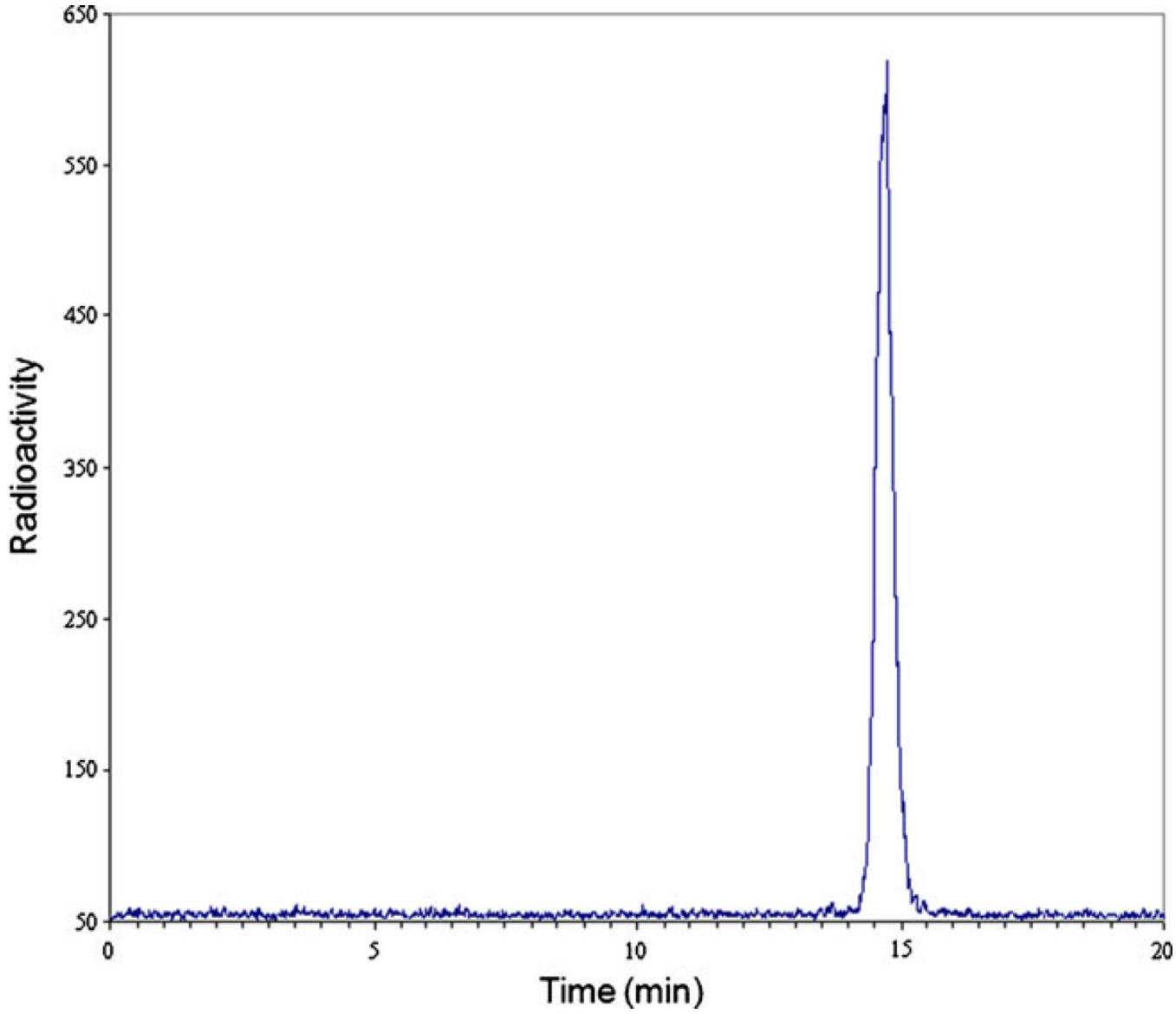

Fig. 2.
A representative radio-HPLC of ^{18}F-FACE after purification: ^{18}F-FACE (99.4%) elution at 14.7 min; ^{18}F-F^{-} (0.6%) elution at 13.7 min.

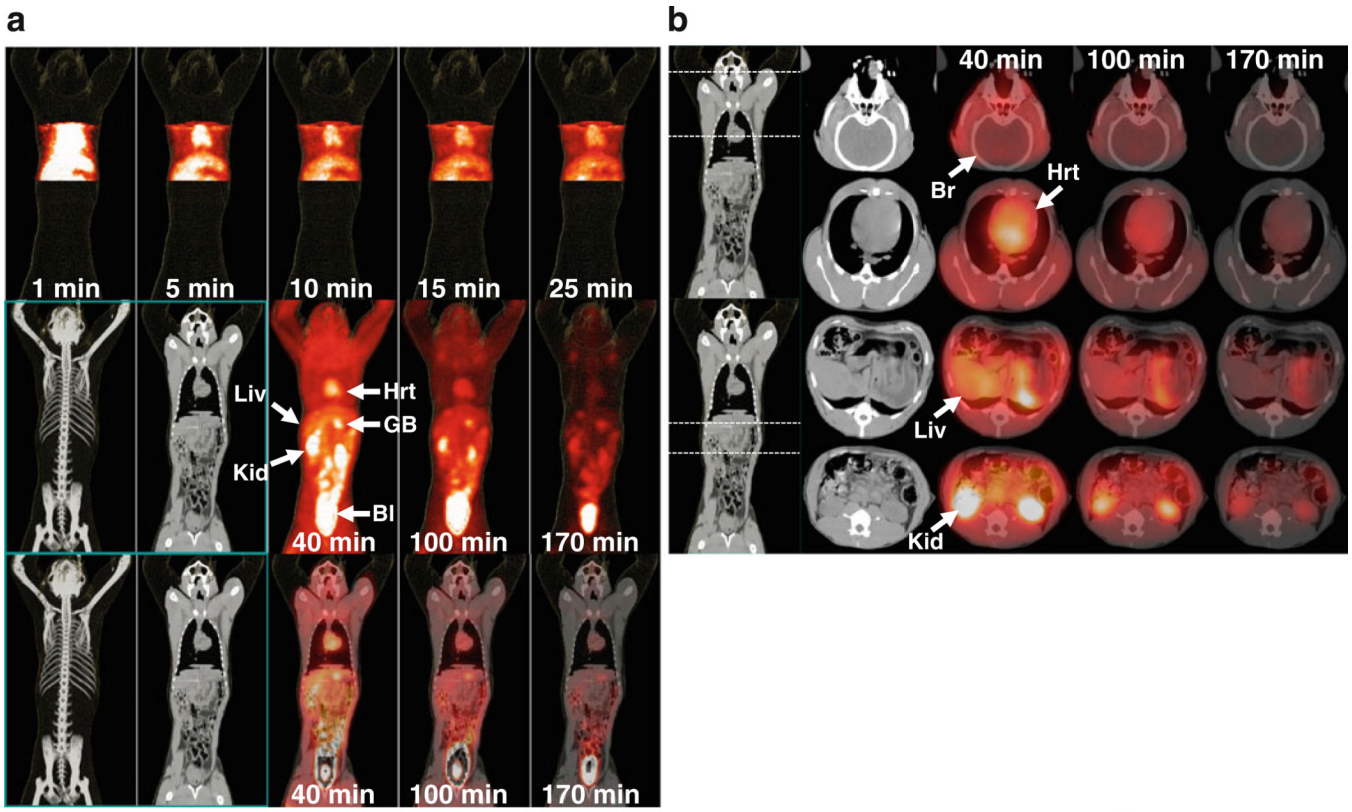

Fig. 3.

PET and PET/CT fusion images obtained at different time points after intravenous injection of ^{18}F-FACE. **a** Coronal maximum intensity projection (MIP) PET images of the thoracoabdominal section obtained at 1–25 min (*top row*); whole-body CT and MIP PET images obtained at 40, 100, and 170 min, average frame times (*middle row*); and corresponding fusion of coronal PET and CT images (*bottom row*). **b** Fusion of axial PET and CT images obtained at the level of the brain (*top row*), heart (*second row*), liver (*third row*), and kidneys (*bottom row*). Different organs are indicated by *arrows* and labeled as: *Br* brain, *Hrt* heart, *Liv* liver, *GB* gall bladder, *Kid* kidney, *Bl* urinary bladder.

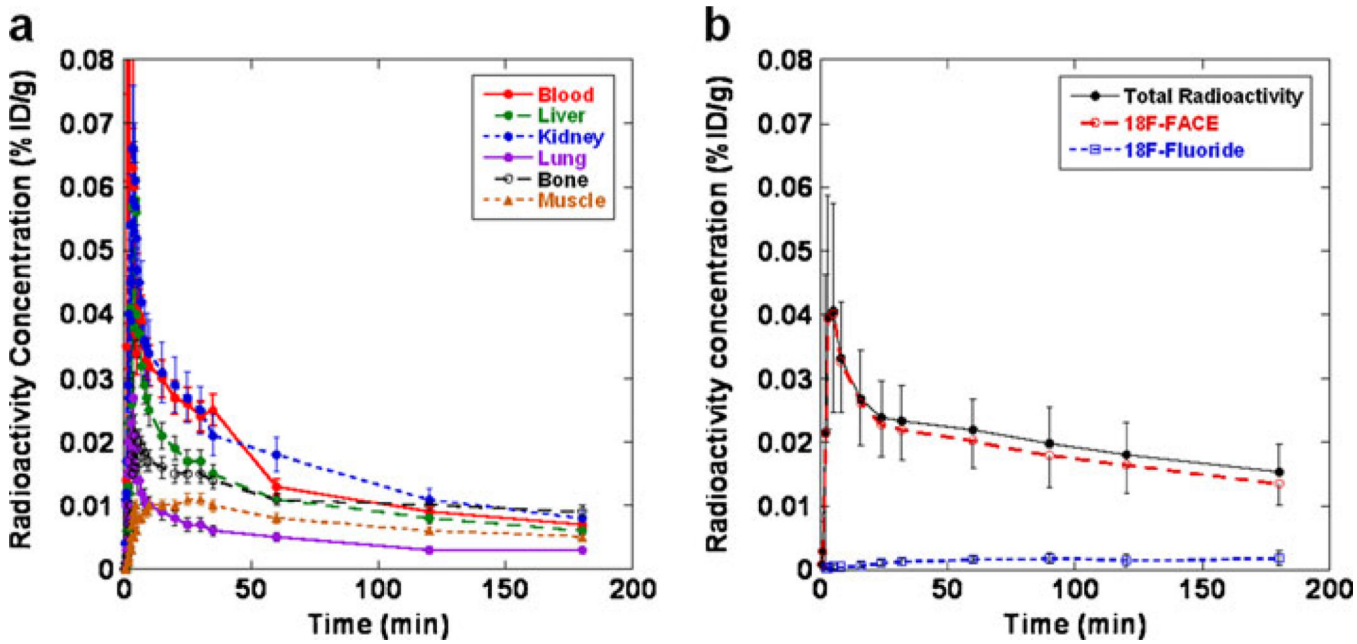

Fig. 4.

Time–activity curves of radioactivity concentration (% ID/g) (**a**) in selected organs and tissues determined from dynamic PET images and (**b**) of intact ^{18}F-FACE and ^{18}F-fluoride in blood plasma after intravenous administration of ^{18}F-FACE in rhesus macaques. Data points: mean±SD.

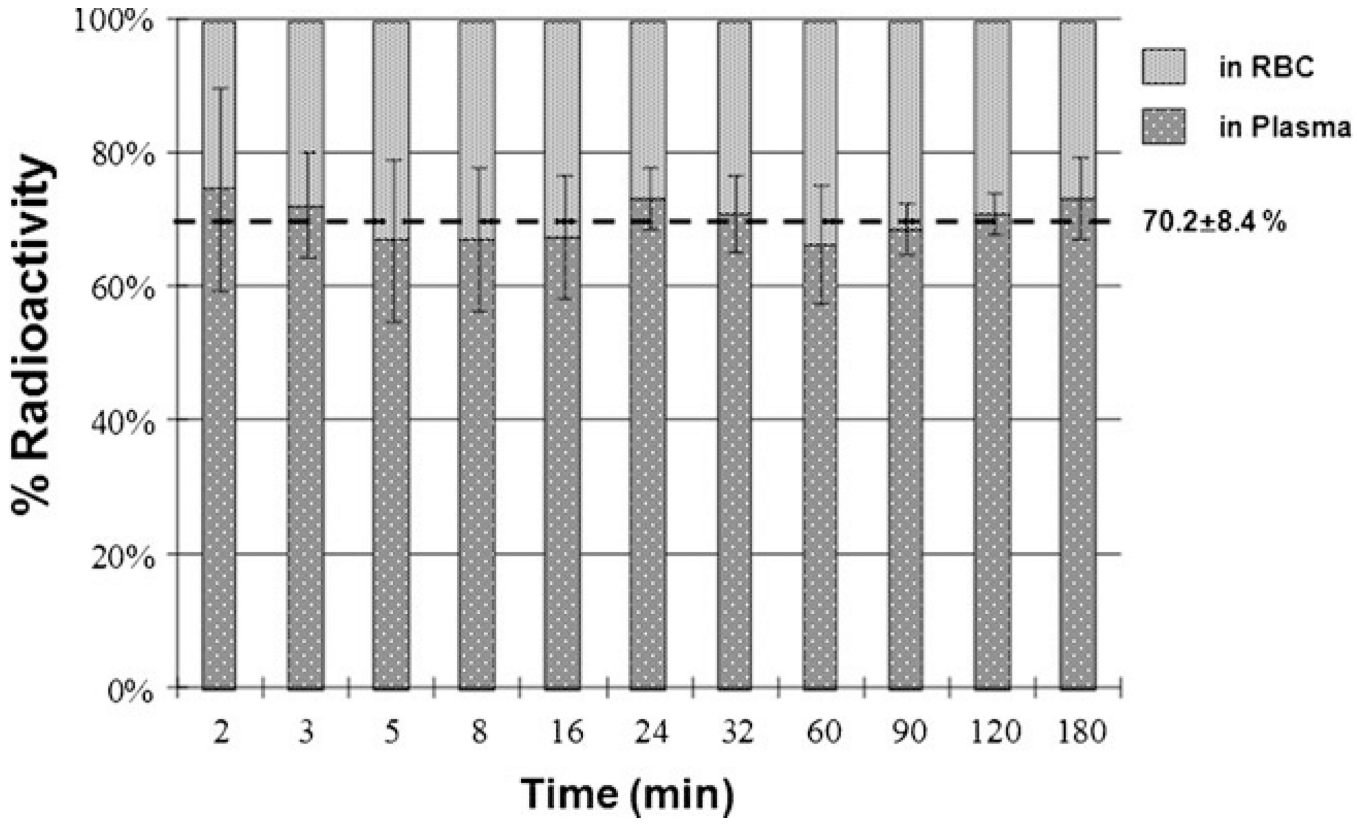

Fig. 5.
Partition of radioactivity in blood between RBC and plasma after injection of ^{18}F-FACE in rhesus macaques.

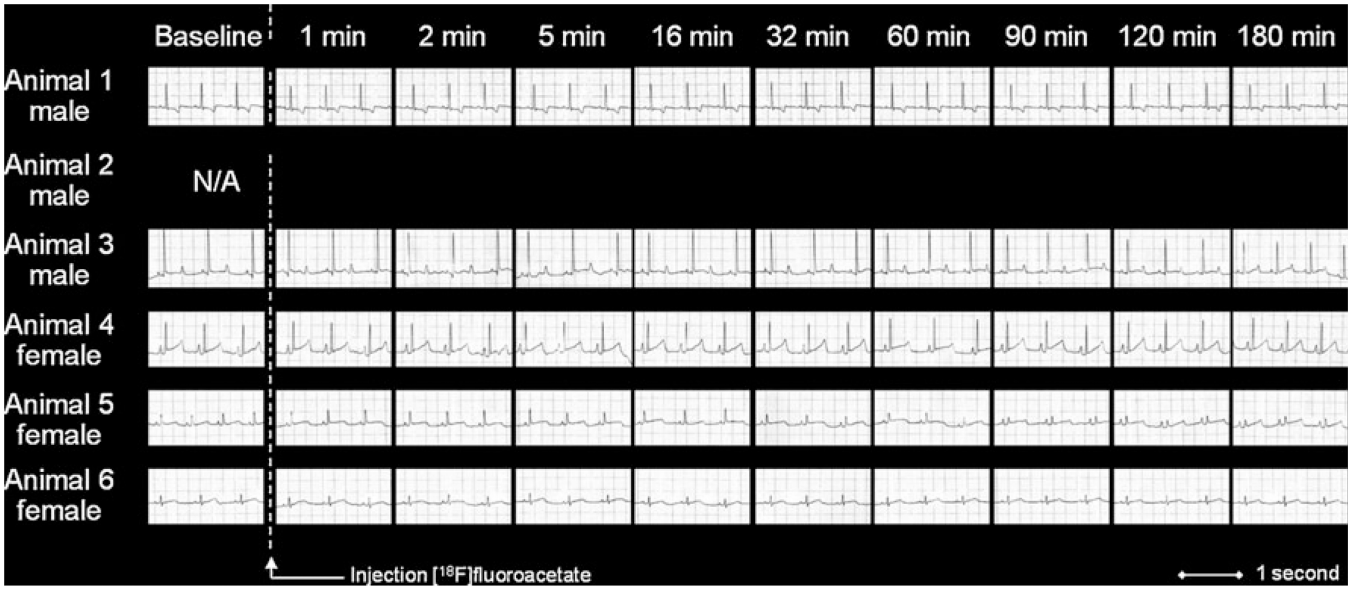

Fig. 6.

Representative ECG profiles of rhesus macaques during ^{18}F-FACE PET imaging study. Quantitative measures of cardiac electrophysiological parameters are provided in Table 2

Table 1

Summary of animal characteristics and hematological profile before PET imaging with ^{18}F-FACE

Animal	Male	Female	All	Normal range
Sex, *n*	3	3	6	
Weight (kg) injected dose	10.1 ±1.8	5.9±0.2	8.00±2.53	N/A
(MBq)	178.3±33.3	152.4±20.4	165.4±28.5	N/A
(MBq/kg)	18.1±5.2	25.9±4.1	21.8±5.9	
Hb (g/dL)	13.2±1.2	12.9±1.1	13.1± 1.0	12.1–14.5
Hct (%)	42.5±4.1	41.6±3.5	42.1±3.4	37.7–44.9
WBC ($\times 10^3$/mL)	7.0±1.0	6.7±1.2	6.8±1.0	6.5–14.7
RBC ($\times 10^6$/mL)	5.8±0.9	5.7±0.7	5.7±0.7	5.3–7.4
Total bilirubin (mg/dL)	0.3±0.1	0.3±0.0	0.3±0.1	0.1–0.4
AST (IU/L)	26.0±9.0	28.0±5.0	27.0±6.7	24.0–52.0
ALT (IU/L)	25.3±6.7	39.0±12.2	32.2±11.5	25.0–52.0
ALP (IU/L)	134.7±62.7	197.0±57.4	165.8±63.7	78–287
Total protein (g/dL)	7.0±0.8	7.1±0.6	7.1±0.7	7.2–8.2
Albumin (g/dL)	4.1±0.3	3.9±0.9	4.0±0.6	3.8–5.0
Blood glucose (mg/dL)	69.0±7.1	63.0±8.0	65.4±7.4	51.0–89.0
Creatinine (mg/dL)	1.1±0.1	1.3±0.4	1.2±0.3	0.7–1.2
BUN (mg/dL)	18.1±3.3	16.2±5.5	17.1±4.2	16.0–25.0

Table 2

Quantitative measures of ECG parameters at different times before and during ^{18}F-FACE PET imaging

	Time (min)									
	Baseline	**1**	**2**	**5**	**16**	**32**	**60**	**90**	**120**	**180**
Heart rate[a]	92±12	88±8	88±8	88±7	87±6	89±7	89±7	87±5	88±3	93±8
p[b]	0.05±0.01	0.04±0.01	0.04±0.00	0.04±0.01	0.05±0.01	0.05±0.01	0.04±0.00	0.04±0.01	0.04±0.01	0.04±0.01
PR	0.11 ±0.01	0.11 ±0.01	0.11 ±0.01	0.11 ±0.02	0.10±0.01	0.11 ±0.01	0.11 ±0.01	0.11 ±0.01	0.11 ±0.01	0.10±0.01
QRS	0.04±0.01	0.05±0.01	0.04±0.00	0.04±0.01	0.04±0.00	0.04±0.00	0.04±0.01	0.04±0.00	0.05±0.01	0.04±0.00
QT	0.35±0.06	0.35±0.04	0.34±0.05	0.35±0.04	0.34±0.04	0.34±0.03	0.34±0.04	0.34±0.03	0.33±0.03	0.34±0.03
ST	0.80±0.74	0.80±0.45	1.00±0.50	0.95±0.51	0.80±0.41	0.60±0.38	0.70±0.54	0.70±0.54	0.60±0.38	0.85±0.63

[a] Heart hare is in per minute

[b] ECG measurements are in seconds

Table 3

Comparison of hematological parameters before and after ^{18}F-FACE PET imaging

Parameter	Before imaging	After imaging	After 1–3 months
Hb (g/dL)	13.1± 1.0	13.1± 1.2*	13.4±0.4*
Hct (%)	42.1±3.4	41.4±2.5*	42.4±2.0*
WBC (×10^3/mL)	6.8±1.0	6.8± 1.1*	4.8±0.5*
RBC (×10^6/mL)	5.7±0.7	5.7±0.6*	5.7±0.1*
Plt (×10^6/mL)	327.3±57.6	328.1±54.2*	303.0±118.8*
Total bilirubin (mg/dL)	0.3±0.1	0.3±0.1*	0.2±0.1*
AST (IU/L)	27.0±6.7	29.0±5.6*	28.7±3.4*
ALT (IU/L)	32.2±11.5	34.2±12.2*	30.5±8.5*
ALP (IU/L)	165.8±63.7	169.4±61.3*	134.0±58.2*
Total protein (g/dL)	7.1±0.7	7.0±0.5*	6.1±0.9*
Albumin (g/dL)	4.0±0.6	3.9±0.8*	3.4±0.8*
BUN (mg/dL)	17.1±4.2	17.9±4.6*	17.9±4.9*

* p>0.1, no statistically significant differences

Table 4

Humanized residence time (in hours) from rhesus macaques after intravenous administration of ^{18}F-FACE

Source organ	Male			Female			All	Male	Female
	1	2	3	4	5	6	Mean±SD	Mean±SD	Mean±SD
Heart	0.048	0.057	0.025	0.039	0.016	0.017	0.034±0.017	0.043±0.016	0.024±0.013
Liver	0.505	0.290	0.065	0.226	0.078	0.093	0.209±0.171	0.287±0.220	0.132±0.082
Kidneys	0.061	0.038	0.043	0.032	0.059	0.030	0.044±0.013	0.047±0.012	0.041±0.016
Intestines[a]	0.235	0.426	0.540	0.261	0.256	0.196	0.319±0.134	0.400±0.154	0.228±0.036
Gall bladder	0.006	0.009	–	0.017	0.014	–	0.011±0.005	0.007±0.002	0.016±0.002
Remainder of body	1.706	1.668	1.960	1.138	1.804	2.228	1.751±0.363	1.778±0.159	1.724±0.549

[a] Assigned in thirds to the small intestine, upper large intestine, and lower large intestine, respectively

Table 5

Organ doses to the 70 kg adult human model in OLINDA/EXM 1.1 using humanized time-integrated activity coefficients from rhesus macaques after intravenous administration of ^{18}F-FACE (mSv/MBq)

Target organ	Male			Female			All	Male	Female
	1	2	3	4	5	6	Mean±SD	Mean±SD	Mean±SD
Adrenals	0.016	0.014	0.013	0.010	0.012	0.013	0.013±0.002	0.014±0.002	0.012±0.002
Brain	0.007	0.007	0.009	0.005	0.008	0.010	0.008±0.002	0.008±0.001	0.007±0.002
Breasts	0.008	0.008	0.008	0.005	0.008	0.009	0.008±0.001	0.008±0.001	0.007±0.002
Gallbladder wall	0.031	0.033	0.017	0.040	0.036	0.016	0.029±0.010	0.027±0.008	0.031±0.013
LLI wall	0.058	0.096	0.120	0.060	0.062	0.052	0.075±0.027	0.091±0.031	0.058±0.005
Small intestine	0.031	0.045	0.055	0.029	0.031	0.029	0.037±0.011	0.044±0.012	0.030±0.002
Stomach wall	0.013	0.013	0.014	0.009	0.012	0.013	0.012±0.002	0.013±0.001	0.011±0.002
ULI wall	0.045	0.071	0.088	0.045	0.047	0.040	0.056±0.019	0.068±0.021	0.044±0.003
Heart wall	0.035	0.038	0.020	0.027	0.015	0.017	0.025±0.010	0.031±0.010	0.019±0.006
Kidneys	0.046	0.032	0.034	0.026	0.042	0.026	0.034±0.008	0.037±0.008	0.031±0.010
Liver	0.067	0.041	0.014	0.032	0.015	0.017	0.031±0.021	0.040±0.026	0.021 ±0.009
Lungs	0.011	0.010	0.010	0.007	0.009	0.011	0.010±0.002	0.010±0.001	0.009±0.002
Muscle	0.010	0.010	0.011	0.007	0.010	0.011	0.010±0.002	0.010±0.001	0.009±0.002
Ovaries	NA	NA	NA	0.013	0.017	0.018	0.016±0.002	N/A	0.016±0.002
Pancreas	0.016	0.014	0.014	0.010	0.013	0.014	0.013±0.002	0.015±0.001	0.012±0.002
Red marrow	0.011	0.011	0.012	0.007	0.010	0.011	0.010±0.002	0.011±0.001	0.009±0.002
Osteogenic cells	0.014	0.014	0.016	0.010	0.014	0.017	0.014±0.003	0.015±0.001	0.014±0.004
Skin	0.007	0.007	0.008	0.005	0.007	0.009	0.007±0.001	0.008±0.001	0.007±0.002
Spleen	0.012	0.011	0.012	0.008	0.011	0.013	0.011±0.002	0.012±0.001	0.010±0.003
Testes	0.009	0.009	0.010	NA	NA	NA	0.009±0.001	0.009±0.001	NA
Thymus	0.010	0.010	0.010	0.007	0.009	0.011	0.010±0.002	0.010±0.001	0.009±0.002
Thyroid	0.009	0.009	0.010	0.006	0.009	0.011	0.009±0.002	0.009±0.001	0.009±0.003
Urinary bladder wall	0.042	0.015	0.017	0.014	0.017	0.021	0.021±0.010	0.025±0.015	0.017±0.004
Uterus	NA	NA	NA	0.011	0.014	0.016	0.014±0.003	NA	0.014±0.003
Total body	0.012	0.012	0.012	0.008	0.010	0.012	0.011±0.002	0.012±0.001	0.010±0.002
EDE	0.024	0.027	0.030	0.019	0.021	0.019	0.023±0.004	0.027±0.003	0.020±0.001

Target organ	Male			Female			All	Male	Female
	1	2	3	4	5	6	Mean±SD	Mean±SD	Mean±SD
ED	0.022	0.025	0.028	0.016	0.018	0.018	0.021±0.004	0.025±0.003	0.018±0.001

EDE effective dose equivalent, *ED* effective dose, *LLI* lower large intestine, *ULI* upper large intestine, *NA* not applicable